

# Simulating the Solar Wind-Magnetosphere Interaction During the Matuyama-Brunhes Paleomagnetic Reversal

Fan Gong<sup>1,2</sup>, Yiqun Yu<sup>1,2\*</sup>, Jinbin Cao<sup>1,2\*</sup>, Yong Wei<sup>3\*</sup>, Jiawei Gao<sup>3</sup>, Hui Li<sup>4</sup>,  
Binzheng Zhang<sup>5</sup>, Aaron Ridley<sup>6</sup>

<sup>1</sup> School of Space and Environment, Beihang University, Beijing, China

<sup>2</sup> Key Laboratory of Space Environment Monitoring and Information Processing, Ministry of Industry and Information Technology, Beijing, China

<sup>3</sup> Institute of Geology and Geophysics, Chinese Academy of Sciences, Beijing, China

<sup>4</sup> State Key Laboratory of Space Weather, National Space Science Center, Chinese Academy of Sciences, Beijing, China

<sup>5</sup> Department of Earth Sciences, the University of Hong Kong, Hong Kong, China

<sup>6</sup> Department of Climate and Space Sciences and Engineering, University of Michigan, Ann Arbor, MI, USA

†Corresponding author: Y. Yu (yiqunyu17@gmail.com),

J. B. Cao (jbcao@buaa.edu.cn),

Y. Wei (weiy@mail.iggcas.ac.cn)

## Key Points:

- We simulate the solar wind-magnetosphere interactions during the Matuyama-Brunhes reversal event with the Space Weather Modeling Framework
- During the reversal, the magnetosphere shrinks, and the transmission efficiency of solar wind power increases up to 18%
- Multiple magnetic reconnection sites open up channels of solar wind power transmission globally.

This is the author manuscript accepted for publication and has undergone full peer review but has not been through the copyediting, typesetting, pagination and proofreading process, which may lead to differences between this version and the [Version of Record](#). Please cite this article as [doi: 10.1029/2021GL097340](https://doi.org/10.1029/2021GL097340).

This article is protected by copyright. All rights reserved.

## **Abstract**

During a paleomagnetic reversal, Earth's geomagnetic field is about 10% of today's magnitude and its topology is far more complex than dipolar. Revealing the solar wind energy transmission during the reversal is of importance for understanding the historic space environment. Using a global MHD model implemented with a data-reconstructed time-dependent paleomagnetic field, this study simulates the solar wind-magnetosphere interactions during the last Matuyama-Brunhes reversal that occurred about 780,000 years ago. As the magnetosphere shrinks in the midst of the reversal, the stand-off distance of the subsolar magnetopause approaches as close as 3 Re. Moreover, multiple magnetic reconnection sites emerge due to the irregular geomagnetic configuration, opening up many channels on the magnetopause surface for the solar wind to directly access. The power transmission efficiency through the magnetopause increases to 18%.

## **Plain Language Summary**

Earth's dynamo at the core produces the intrinsic geomagnetic field that helps prevent solar wind from directly impacting the atmosphere. We present simulation results on the evolution of the space environment during the Matuyama-Brunhes event that occurred about 780,000 years ago and show that the protection was weakened in two ways: the reduction of the size of the magnetosphere and the increase of power input efficiency. The stand-off distance of the subsolar magnetopause during the polarity reversal approaches as close as 3 Re. Due to the irregular magnetic field configuration, multiple channels for solar wind energy appear on the magnetosphere, increasing the power transmission efficiency through the magnetopause up to 18%. This implies that many satellites may become more vulnerable to solar storms if a new reversal is underway.

## 1 Introduction

The terrestrial magnetosphere is formed due to the interaction between the solar wind and the geomagnetic field. In addition to the time-varying solar wind conditions, the intrinsic magnetic field plays a crucial role in shaping the magnetosphere. Paleomagnetic measurements show that the Earth's magnetic field varies greatly, with the most dramatic changes being polarity reversals that take place on average every ~200,000 years (e.g., Merrill & McFadden, 1999). During the polarity reversal period, the shape and size of the magnetosphere changes (Siscoe & Chen, 1975; Glassmeier et al., 2004; Tarduno et al. 2010), and the magnetic shielding of the atmosphere to direct solar wind entry may be lower than today (Glassmeier, et al., 2009; Glassmeier & Vogt, 2010; Olson et al., 2011). Wei et al. (2014) even found that the ionospheric O<sup>+</sup> escape rate during the reversal, estimated from a modified Martian ion escape model, could increase by 3-4 orders of magnitude. While it is established that reversals could last for ~1,000–8,000 years (Clement, 2004), the exact duration of the reversals and the variations therein are uncertain. A recent study by Singer et al., (2019) proposed a complex 22 thousand-year (kyr) long transition for the Matuyama-Brunhes boundary, spanning approximately from 795 to 773 thousand years ago (ka).

Although the understanding of geomagnetic reversals has been improved considerably over the years with paleomagnetic studies and geodynamic simulations, the geomagnetic properties during a polarity transition, especially the dominance of dipolar or multipolar components, are still uncertain (Jacobs, 1994; Valet et al., 2012; Valet & Fournier, 2016). It has been suggested that the dipole moment is reduced and the high-order multipoles are significant during the last Matuyama-Brunhes reversal (Leonhardt and Fabian, 2007; Singer et al., 2019). In order to understand how the geomagnetic field changes in the reversal period influence the magnetospheric configuration and impact on the geospace environment, previous studies have used simplified geomagnetic field configuration for the transitional reversal time. For example, by appropriately scaling today's geomagnetic field models, Vogt and Glassmeier (2001) provided scaling relations for magnetospheric current systems. Such a method of using a scaled dipole

field is further used in other studies to examine the magnetosphere-ionosphere coupling and the dependences on the interplanetary magnetic field (IMF) (e.g., Zieger et al., 2006a, 2006b). Wang et al. (2017) found that reduced geomagnetic fields generally lead to an increase of the thermospheric mass density but a decrease of electron density at auroral latitudes. Some studies also investigated the effects of equatorial dipole magnetosphere (Zieger et al., 2004) or quadrupole configurations (Vogt et al., 2004, 2007) and suggested that high-energy particles in the MeV range are more likely to penetrate to about 40° altitude atmosphere during the reversal. In recent years, a superposition of dipole and quadrupole fields has been proposed to be a possible representation during a geomagnetic reversal (Glassmeier & Vogt, 2010; Tsareva et al., 2019). Stadelmann et al. (2010) considered several possible combinations of dipole and quadrupole paleomagnetic fields (including axisymmetric paleomagnetic fields) and illustrated the particle (in the GeV range) impact regions and cutoff latitudes against kinetic energy.

However, neither the scaled/reduced dipole fields nor multipole fields can realistically represent the paleomagnetic field during the polarity reversal. Therefore, in order to reveal the solar wind-magnetosphere interaction during the reversal stage, we use a global MHD model implemented with a more realistic intrinsic geomagnetic field, which is characterized by the data-reconstructed model “IMMAB4 (final inverse model of Matuyama-Brunhes)” (Leonhardt & Fabian, 2007). The Space Weather Modeling Framework (SWMF) model is used to simulate the last Matuyama-Brunhes (M-B) reversal and explore how the energy transfer from the solar wind into the magnetosphere is dependent on the structure and strength of the intrinsic field.

## **2 Methodology**

### **2.1 Model Description**

To simulate the solar wind-magnetosphere interaction during the paleomagnetic reversal, we use the SWMF (Tóth et al., 2005, 2012) that integrates several first-principle physics-based models, including a global MHD model Block-Adaptive Tree

Solar-wind Roe Upwind Scheme (BATS-R-US) (Powell et al., 1999) and an ionospheric potential solver (Ridley et al., 2004). The integrated model is suitable for solving the geospace circulation dynamics and has been extensively validated (e.g., Wang et al. 2008; Yu & Ridley, 2008; Yu et al., 2010, 2015, 2017; Ridley et al., 2016).

The BATS-R-US code solves the global magnetospheric using ideal MHD equations from the upstream solar wind to the magnetosphere with the inner boundary at  $r = 2.0$  Re and the upstream outer boundary at  $32$  Re. For  $r < 4$  Re, the spatial resolution is  $1/8$  Re, and the outer region has a coarser resolution (e.g.,  $1/4$  Re for  $r < 8$  Re). The electric potential is obtained based on constant conductance ( $\Sigma_P=4.0$ ,  $\Sigma_H=0.25$ ) and field alignment currents (FACs) calculated at  $r = 2.5$  Re and mapped to the ionosphere. The electric potential is used to specify the inner boundary velocity of the MHD code.

## 2.2 Setup of Paleomagnetic field and solar wind conditions

The last geomagnetic reversal, i.e., the Matuyama-Brunhes reversal, occurred approximately 780,000 years ago. Based on paleomagnetic data, Leonhardt and Fabian (2007) developed a Bayesian inversion technique to reconstruct the spherical harmonic expansion of the transitional field from 795 ka to 764 ka. Their data-reconstructed model “IMMAB4” can be used to specify the geomagnetic field at any location in space for the M-B reversal. But one caveat of the model should be noted that it may not represent the complete complexity of the M-B reversal because it ultimately relies on sparse global data coverage, and the M-B reversal may not fully represent the behavior of reversals overall.

We implement the corresponding spherical harmonic coefficients of “IMMAB4” in BATS-R-US (see supporting materials for these coefficients in Table S1 and comparisons of different components in Figure S1). Due to the limitation of high-resolution data, only the interval between 782 ka and 767 ka is relatively reliable with sufficient data coverage. Singer et al., (2019) proposed in a recent study that the M-B reversal was complicated with various magnetic field changes from 795 to 773 ka. Therefore, in order to attain a more reliable field from the IMMAB4 model, we mainly

focus on three different phases of the reversal period within 782ka and 773ka (Figure 1).

At 794 ka, the geomagnetic field is approximately a dipole with its magnetic north pole in the northern hemisphere. At 765 ka, the magnetic north pole is in the southern hemisphere, similar to today's configuration. At these two phases, the dipolar components of the Earth's magnetic field are  $\sim 8.78 \times 10^{22}$  A m<sup>2</sup> and  $\sim 9.15 \times 10^{22}$  A m<sup>2</sup>, respectively, both slightly larger than in AD 2020 at  $7.70 \times 10^{22}$  A m<sup>2</sup> (Alken et al., 2021). However, in the midst of the reversal (i.e., 774.5 ka), the geomagnetic field no longer exhibits a dipole field, but rather a more complicated and irregular configuration. Local magnetic field loops occur within the same hemisphere. At this epoch, the dipolar field component is  $\sim 4.78 \times 10^{21}$  A m<sup>2</sup>, only about 5.5% of that prior to the reversal.

The M-B reversal event lasted for around 22 kyr, much longer than the 11-year solar cycle (Friis-Christensen & Lassen, 1991). We, therefore, drive the BATS-R-US model with constant solar wind and IMF conditions during the paleomagnetic reversal, assuming that the fluctuations in interplanetary conditions are negligible within such a long era. We set the solar wind conditions with  $V_{xsw} = 400$  km/s,  $N_{sw} = 5$  cm<sup>-3</sup>,  $T = 10^5$  K, and IMF  $B_z = -10$  nT, while  $V_{y,sw} = V_{z,sw} = 0$  km/s, and  $B_x = B_y = 0$  nT. With such driving conditions, we conduct 20 simulations from 794 ka to 765 ka, each embedded with a specific intrinsic geomagnetic field determined from the spherical harmonic model "IMMAB4". Each simulation is run for 100,000 steps to arrive at a steady state of the magnetosphere.

### 2.3 Calculation of Energy Transfer through the Magnetopause

To understand the solar wind-magnetosphere interaction during the reversal, we apply a streamlined method similar to Palmroth et al. (2003) and Wang et al. (2014) to identify the magnetopause surface and then estimate the power transfer of the solar wind across the surface.

The total power gain through the magnetopause ( $SWP_{m.p.}$ ) is defined as follows (Palmroth et al., 2003):

$$SWP_{m.p.} = \int dW_p + \int dW_m = \int dS(\mathbf{K}_p) \cdot \hat{\mathbf{n}} + \int dS(\mathbf{K}_m) \cdot \hat{\mathbf{n}} \quad (1)$$

where  $W_m$  is the mechanical power,  $W_p$  is the electromagnetic power,  $dS$  is the area of the surface element,  $\hat{\mathbf{n}}$  is the normal unit vector,  $\mathbf{K}_p$  is the electromagnetic energy flux (i.e., Poynting vector), and  $\mathbf{K}_m$  is the mechanical energy flux. These energy fluxes are defined as

$$\mathbf{K}_p = \frac{1}{\mu_0} \mathbf{E} \times \mathbf{B} \quad (2)$$

$$\mathbf{K}_m = \left( U + P - \frac{B^2}{2\mu_0} \right) \mathbf{V} \quad (3)$$

where  $P$  is the thermal pressure,  $\mathbf{B}$  is the magnetic field just outside of the magnetopause,  $\mathbf{V}$  is the velocity,  $\mathbf{E}$  is the electric field, and  $U$  is the total energy density, defined as

$$U = \frac{P}{\gamma - 1} + \frac{1}{2} \rho V^2 + \frac{B^2}{2\mu_0} \quad (4)$$

The above three terms on the right are the thermal energy density, kinetic energy density, and magnetic energy density, respectively, with  $\gamma = 5/3$  the polytropic index, and  $\rho$  the mass density. The total power gain through the magnetopause ( $SWP_{m.p.}$ ) is calculated by integrating the energy flux (i.e.,  $\mathbf{K}_p$  and  $\mathbf{K}_m$ ) above the entire magnetopause surface from the subsolar magnetopause to  $X_{GSM} = -40$  Re in the tail. The positive value indicates inward energy transfer through the magnetopause, and vice versa. In addition, the total kinetic energy of the solar wind impinging on the magnetopause per unit time, or the total effective solar wind power ( $SWP_e$ ), can be calculated as (Han et al., 2014):

$$SWP_e = \frac{1}{2} \rho_{sw} V_{sw}^3 A \quad (5)$$

where  $A$  is the projected cross-section area of the magnetopause surface in the YZ plane,  $\rho_{sw}$  and  $V_{sw}$  are the upstream (non-disturbed) solar wind mass density and velocity, respectively.

### 3 Result

Figure 2 (left) shows a 3D view of the magnetopause surface at different phases during the M-B reversal. The magnetosphere shrinks while undergoing the geomagnetic field reversal, and expands again after the reversal. Figure 2 (right) shows the 3D magnetic field configuration. Before 776 ka, magnetic reconnection occurs at high latitudes where the diverted southward IMF is antiparallel to the Earth's magnetic field. As the reversal progresses, the magnetopause gradually approaches the Earth while the high-latitude magnetic reconnection remains because the geomagnetic field is still manifested as a dipolar field, despite the weakened magnetic field strength. As the size of the magnetosphere decreases, the geomagnetic field exhibits an irregular configuration and many geomagnetic field lines loop locally within the same hemisphere, for example at 774.5 ka. Multiple reconnection sites emerge where the local “dipolar loops” encounter the antiparallel IMF. When the geomagnetic field slowly turns back into a normal dipole, the reconnection appears on the dayside magnetopause as well as in the magnetotail (i.e., at 773.5 ka), allowing for the familiar Dungey configuration (Dungey, 1961). Under such a state, the magnetosphere continues its expansion as the magnitude of the dipole gradually strengthens.

As illustrated in Figure 3(a), the magnetosphere experiences three distinct stages during this polarity reversal event: pre-reversal phase before 779 ka, reversal phase (779ka - 769ka), and post-reversal phase after 769 ka. In the pre-reversal phase, the stand-off distance of the subsolar point of the magnetosphere smoothly but monotonically decreases from 10 Re to 7 Re, while in the post-reversal phase, the subsolar point gradually migrates outward from 6 Re. In between the two phases, the stand-off distance undergoes drastic changes: rapidly dropping from 7 Re to 3 Re first, and then increasing to 4.5 Re at 774 ka, followed by a quasi-steady “plateau” period for about 2.5 kyr before increasing to 6 Re again. Such a complicated reaction of the



magnetosphere indicates that the shape of the magnetosphere depends strongly on the intrinsic geomagnetic field.

Figure 3(b) shows that, in the pre-reversal phase, the total solar wind power gain through the magnetopause surface ( $SWP_{m.p.}$ , the results from Equation (1)) remains nearly constantly at a level of  $10^{11}$  W, comparable to today's power transfer under northward IMF conditions (e.g., Lu et al., 2013). It only enhances near the end of this phase at 779 ka. In contrast, as the geomagnetic dipole moment decreases and the magnetosphere shrinks, the effective solar wind power ( $SWP_e$ , the results from Equation (5)) shown in Figure 3(c), representing the upstream solar wind kinetic energy impinging on the maximum cross-section of the magnetopause in the YZ plane, monotonically decreases with the same trend as a dipolar moment but at a time-varying rate. This means that the dipole component has a more significant impact on the Earth's magnetosphere than higher-order components. This pre-reversal  $SWP_e$  at a level of  $10^{13}$  W is consistent with the theory developed in Blackman and Tarduno (2018). The ratio between  $SWP_{m.p.}$  and  $SWP_e$ , that is, the power transmission efficiency gradually increases to 1 % and then briefly fluctuates around 3% near the end of this pre-reversal phase (Figure 3(d)).

During the reversal phase, as the geomagnetic dipole moment is significantly reduced, the  $SWP_e$  in Figure 3(b) dramatically drops to the minimum at 775 ka, and then returns to its previous values, followed by a transitional decrease at 771 ka. After that, it returns to its initial level again. Such variation follows a similar trend of the subsolar stand-off distance. On the other hand, the  $SWP_{m.p.}$  in Figure 3(c) reaches its minimum earlier than the time when the subsolar point shifts to the closest, and then rapidly increases by more than a factor of two until the magnetospheric configuration nearly rests at the "plateau" around 774 ka. Later on, it briefly drops and gradually increases again until 769 ka.

The ratio between the two powers, i.e., the power transmission efficiency in Figure 3(d), dramatically soars from 3% to 18% at 775 ka. The largest percentage occurs when the  $SWP_{m.p.}$  temporarily maximizes. Such high efficiency lasts for about 2.5 kyr before leveling off. This intense power transmission rate appears right in the midst of the

reversal when the intrinsic geomagnetic field is substantially irregular and when multiple channels, due to more reconnection sites, are cut open on the magnetopause surface. Despite the small size of the magnetosphere, more open channels provide the solar wind with more access into the geospace system, and hence a relatively larger efficiency. However, the power transmission efficiency at the two moments (green dash lines) under the similar condition of the  $SWP_{m.p.}$  and the ratio of dipole component to quadrupole component presents a huge difference, which means that the polarity reversal of the dipole component at a later moment (Figure 3(b)) changes the angular with the IMF  $B_z$  in the solar wind that has a significant impact on the power transmission efficiency and the  $SWP_{m.p.}$ . Near the end of the reversal, as the geomagnetic dipole moment grows, the magnetosphere configuration restores to be more dipolar and continues to inflate. Those multiple energy channels on the magnetopause surface gradually disappear, suppressing the pathways for energy transmission, resulting in a decreased power transmission efficiency.

Previous studies reported that for a typical intense geomagnetic storm ( $-300 < SYMH \leq -100$  nT), the largest power transmission efficiency is 11.8%-13.2% (Li et al., 2012; Han et al., 2014). These large efficiencies are highly dependent on the solar wind electric field and dayside reconnection rate (Li et al. 2010). In this study, the peak efficiency is 18%, much larger than that during an intense storm. This suggests that with a paleomagnetic configuration of the polarity reversal, the power transmission efficiency during a magnetic storm is significantly improved.

In the post-reversal phase after 771 ka, the increase of the geomagnetic dipole moment allows the magnetosphere to gradually recover to the pre-reversal size, and both  $SWP_e$  and  $SWP_{m.p.}$  smoothly increase when the magnetopause inflates and encounters more solar wind energy. The  $SWP_{m.p.}$  reaches  $10^{12}$  W, comparable to the level in a normal magnetosphere under southward IMF conditions (e.g., Wang et al., 2014). However, the power transmission efficiency decreases to 10 % and is lower than that during the reversal.

After the solar wind energy transmits through the magnetopause, the amount of energy flowing down to the Earth is of particular importance for the upper atmosphere heating and mass escape (Palmroth et al., 2006). Therefore, we calculate the perturbation Poynting flux  $S_p$  at  $R = 2.5$  Re during the reversal event using the following formula (Vanhamäki et al., 2012):

$$S_p = \frac{1}{\mu_0} \mathbf{E} \times \delta \mathbf{B} \quad (6)$$

where  $\mathbf{E}$  is the electric field, and  $\delta \mathbf{B} = \mathbf{B} - \mathbf{B}_g$  is the magnetic field perturbation, with  $\mathbf{B}_g$  the intrinsic geomagnetic field at  $R = 2.5$  Re.

Figure 4 shows both the downward Poynting flux and the field-aligned currents (FACs)  $J_{||}$  at  $R = 2.5$  Re in the northern hemisphere. Before the polarity reversal at 776 ka, as the magnetic reconnection occurs at high latitudes, a pair of strong NBZ-sense FACs and a pair of weak Region-1-sense FACs emerge near the north pole, similar to today's FACs pattern under northward IMF conditions (Ganushkina et al., 2018). The total downward Poynting flux is relatively small, consistent with northward IMF. During the reversal time at 774.5 ka and 774.2 ka, both FACs and Poynting flux are more intense. The global distribution of FACs and Poynting flux extend across all latitudes, even near the equator. This happens when multiple reconnection sites occur on the magnetopause and the magnetic field configuration is substantially non-dipolar, suggesting that the entire near-Earth environment would have intense energy deposition. After 773.5 ka, a pair of Region-1-sense FACs appears and enhances at high latitudes. Equatorward of that, weak Region-2 FACs are also visible. The Poynting flux flows down towards the Earth dominantly in the polar cap region as well as mid-latitudes at both dawn and dusk. From 768 ka on, both FACs and Poynting flux are consistent with today's nominal Dungey configuration. This marks the restoration of the dipolar configuration and the end of reversal.

The Poynting flux and FACs are more intense after the reversal. As the total energy gain through the magnetopause keeps growing following the expansion of the magnetosphere during the post-reversal period, it is not surprising to see stronger

Poynting flux deposited downward to the Earth's atmosphere since the configuration is similar to southward IMF today. However, during the reversal, the worldwide and irregular energy transfer channels cause the upper atmosphere to have more globally distributed energy sources, meaning that the upper atmosphere probably would experience relatively random heating across the globe. Knowing whether such a condition is favorable for energy dissipation over the entire upper atmosphere is significant for understanding atmospheric expansion and loss. This will be investigated in our future studies.

#### **4 Summary and Discussion**

It has been proposed that the geomagnetic field can positively help with the preservation of the atmosphere (and ultimately the retention of water) through the shielding effect (Tarduno et al., 2014; Blackman & Tarduno 2018). During geomagnetic field reversals, the field is likely to be irregular and weakened (Valet et al., 2012; Bono et al., 2019). Previous numerical studies simply assumed a reduced dipole magnetic moment or multipolar magnetic field to represent the geomagnetic configuration in the polarity reversal. This study incorporates a more realistic paleomagnetic model into a global magnetosphere MHD model BATS-R-US to unveil the solar wind-magnetosphere interactions and associated solar wind energy transfer during the entire M-B reversal event. We also note that the realistic M-B reversal may be more complex than what the model can represent because the paleomagnetic field model highly relied on historic data sets that unfortunately lacked global availability (see more details in Leonhardt and Fabian (2007)).

With the modeling results, some major findings are summarized as follows. Prior to the reversal process, the paleomagnetic field is dipolar with its north pole in the northern hemisphere as its magnetic moment becomes smaller. It then undergoes a period without any clear dipolar structure, with multiple local loop configurations appearing randomly. Finally, the magnetic north pole emerges in the southern hemisphere as the magnetic moment continuously increases.

With such unique changes in the geomagnetic field, the magnetosphere undergoes drastic changes during the reversal. The stand-off distance of the subsolar magnetopause shifts toward the Earth and approaches  $3 R_e$ , as the field weakens. In such a condition, if the solar wind dynamic pressure were to change significantly to further compress the magnetosphere (e.g., during a Coronal Mass Ejections event), the Earth's atmosphere may be directly exposed to the solar wind. It has been discussed whether a smaller or larger magnetosphere can protect the planet's atmosphere (Moore & Horwitz, 2007; Tarduno et al., 2014). Blackman and Tarduno (2018) believed that the competition between inflow velocity (from stellar wind) and collection area (from the magnetosphere) determines whether the magnetosphere can protect the planetary atmosphere. In our work, the polarity reversal of the Earth's intrinsic magnetic field not only changes the size of the magnetosphere but also affects the solar wind power transmission efficiency. According to previous studies, this can undoubtedly affect the protective role of the magnetosphere on the Earth's atmosphere.

In the midst of the reversal, multiple reconnection sites appear where local dipole-like magnetic fields emerge and encounter anti-parallel IMF. The ratio between  $SWP_{m,p}$  and  $SWP_e$  ramps up to 18% and keeps at this high level for about 2.5 kyr. This high efficiency is approximately 10 times larger than the pre-reversal level and twice as much as the post-reversal level, implying that the geomagnetic reversal enables elevated power transmission efficiency. As shown in the in-plane subplot in Figure 3b, we find that the rising of the power transmission efficiency occurs when the quadrupole component of the geomagnetic field is dominant over the dipole component and when the dipole component starts to increase after its declination in the pre-reversal phase. During this time period, the magnetosphere starts to expand gradually with an increasing solar wind energy impinging on the magnetopause, and the dipole component starts to recover as the dominant component with an opposite polarity. These reasons may help increase the magnetic reconnection rate on the dayside and contribute to the enhancement of power transmission efficiency.

Multiple open channels over the magnetopause surface at this stage provide more chances for solar wind energy to enter the magnetosphere and deposit towards the Earth. The enhanced Poynting flux down to the upper atmosphere appears globally, indicating that a large amount of solar wind energy is directly transmitted into the lower latitudes and even equatorial regions, which may suggest global heating of the atmosphere of the Earth. The stand-off distance of the magnetopause compressed to  $3 R_E$  during the M-B reversal, which is within the normal plasmapause boundary in today's terrestrial magnetosphere (Laakso & Jarva, 2001). Therefore, the plasmasphere, filled with cold plasma from the ionosphere, would be greatly affected or may disappear. Moreover, the near-Earth magnetospheric configuration is totally disturbed when the geomagnetic fields are highly non-dipolar. Hence different circumstances would be expected in the ring currents, radiation belts, and other regions that heavily rely on the magnetic field configuration. With regional magnetic loop structures, the drifting charged particles may not be trapped around the Earth. The global-scale ring current may not even exist during the reversal phase as suggested by Vogt and Glassmeier (2000). In the near future, we plan to apply a particle tracing technique to investigate the near-Earth particle motions under the reversal configuration.

## Acknowledgments

This work is supported by the NSFC grants 41821003 and 41974192, by the B-type Strategic Priority Program of the Chinese Academy of Sciences (Grant No. XDB41000000), the pre-research projects on Civil Aerospace Technologies No. D020103 and D020105 funded by China's National Space Administration (CNSA). This work was carried out using the SWMF and BATS-R-US tools developed at the University of Michigan's Center for Space Environment Modeling (CSEM). Simulations were performed over the Tianhe-2 National Supercomputer Center at Guangzhou, China.

## Data Availability Statement

Open research: The modeling tools described in this publication are available online: <https://github.com/MSTEM-QUDA>. The input parameter file for the BATS-R-US MHD model and resulted simulation data are all available at <https://doi.org/10.5281/zenodo.4628624>.

## References

Alken, P., Thébault, E., Beggan, C. D., Amit, H., Aubert, J., Baerenzung, J., et al. (2021). International Geomagnetic Reference Field: the thirteenth generation. *Earth, Planets and Space*, 73, 1880-5981. <https://doi.org/10.1186/s40623-020-01288-x>

Blackman, E. G., & Tarduno, J. A. (2018). Mass, energy, and momentum capture from stellar winds by magnetized and unmagnetized planets: implications for atmospheric erosion and habitability. *Monthly Notices of the Royal Astronomical Society*, 481, 4, 5146–5155. <https://doi.org/10.1093/mnras/sty2640>

Bono, R.K., Tarduno, J.A., Nimmo, F., & Cottrell, R.D. (2019). Young inner core inferred from Ediacaran ultra-low geomagnetic field intensity, *Nature Geoscience*, 12, 143-147. <https://doi.org/10.1038/s41561-018-0288-0>

Clement, B. M. (2004). Dependence of the duration of geomagnetic polarity reversals on site latitude. *Nature*, 428(6983), 637–640. <https://doi.org/10.1038/nature02459>

Dungey, J. W. (1961), Interplanetary Magnetic Field and the Auroral Zones. *Physical Review Letters*, 6(2), 47-48. <https://doi.org/10.1103/PhysRevLett.6.47>

Friis-Christensen, E., & Lassen, K. (1991). Length of the solar cycle: An indicator of solar activity closely associated with climate. *Science*, 254(5032), 698–700. <https://doi.org/10.1126/science.254.5032.698>

Ganushkina, N. Y., Liemohn, M. W., & Dubyagin, S. (2018). Current systems in the Earth's magnetosphere. *Reviews of Geophysics*, 56, 309–332. <https://doi.org/10.1002/2017RG000590>

Glassmeier, K. H., Richter, O., Vogt, J., Mobus, P., & Schwalb, A. (2009). The sun, geomagnetic polarity transitions, and possible biospheric effects: Review and illustrating model. *International Journal of Astrobiology*, 8(3), 147–159. <https://doi.org/10.1017/S1473550409990073>

Glassmeier, K. H., & Vogt, J. (2010). Magnetic polarity transitions and biospheric effects. *Space Science Reviews*, 155, 387–410. <https://doi.org/10.1007/s11214-010-9659-6>

Glassmeier, K., Vogt, J., Stadelmann, A., & Buchert, S. (2004). Concerning long-term geomagnetic variations and space climatology. *Annales Geophysicae*, 22, 3669–3677. <https://doi.org/10.5194/angeo-22-3669-2004>

Han, J. P., Wang, C., & Li, H. (2014), Energetics characteristics of the super magnetic storm on November 20, 2003 based on 3D global MHD simulation. *Science China: Earth Sciences*, 57, 3035–3046. <https://doi.org/10.1007/s11430-014-5013-2>

Jacobs, J. A. (1994), *Reversals of the Earth's Magnetic Field*. Cambridge University Press, New York. <https://doi.org/10.1017/CBO9780511524929>



Laakso, H., & Jarva, M. (2001) Evolution of the plasmopause position. *Journal of Atmospheric and Solar-Terrestrial Physics*, 63(11), 1171-1178. [https://doi.org/10.1016/S1364-6826\(01\)00008-6](https://doi.org/10.1016/S1364-6826(01)00008-6)

Leonhardt, R., & Fabian, K. (2007). Paleomagnetic reconstruction of the global geomagnetic field evolution during the Matuyama/Brunhes transition: Iterative Bayesian inversion and independent verification. *Earth and Planetary Science Letters*, 253, 172–195. <https://doi.org/10.1016/j.epsl.2006.10.025>

Li, H., Wang, C., & Kan, J. R. (2010). Midday magnetopause shifts earthward of geosynchronous orbit during geomagnetic superstorms with  $Dst \leq -300$  nT. *Journal of Geophysical Research*, 115, A08230, <https://doi.org/10.1029/2009JA014612>

Li, H., Wang, C., Xu, W. Y., & Kan, J. R. (2012). Characteristics of magnetospheric energetics during geomagnetic storms. *Journal of Geophysical Research: Space Physics*, 117, A04225, <https://doi.org/10.1029/2012JA017584>

Lowes, F. J. (1966). Mean-square values on sphere of spherical harmonic vector fields. *Journal of Geophysical Research*, 71(8), 2179, <https://doi.org/10.1029/JZ071i008p02179>

Lu, J. Y., Jing, H., Liu, Z. Q., Kabin, K., & Jiang, Y. (2013). Energy transfer across the magnetopause for northward and southward interplanetary magnetic fields. *Journal of Geophysical Research: Space Physics*, 118, 2021–2033. <https://doi.org/10.1002/jgra.50093>

Merrill, R.T. & McFadden, P.L. (1999). Geomagnetic polarity transitions. *Reviews of Geophysics*, 37(2), 201– 226. <https://doi.org/10.1029/1998RG900004>

Moore, T.E., & Horwitz, J.L. (2007) Stellar ablation of planetary atmospheres. *Reviews of Geophysics*, 45 (3), art. no. RG3002. <https://doi.org/10.1029/2005RG000194>

Olson, P. L., Glatzmaier, G. A., & Coe, R. S. (2011). Complex polarity reversals in a geodynamo model. *Earth and Planetary Science Letters*, 304(1-2), 168–179. <https://doi.org/10.1016/j.epsl.2011.01.031>

Palmroth, M., Laitinen, T. V., & Pulkkinen, T. I. (2006). Magnetopause energy and mass transfer: results from a global MHD simulation, *Annales Geophysicae*, 24, 3467–3480. <https://doi.org/10.5194/angeo-24-3467-2006>

Palmroth, M., Pulkkinen, T. I., Janhunen, P., & Wu, C. C. (2003). Stormtime energy transfer in global MHD simulation. *Journal of Geophysical Research: Space Physics*, 108, 1048. <https://doi.org/10.1029/2002JA009446>

Powell, K. G., Roe, P. L., Linde, T. J., Gombosi, T. I., & Zeeuw, D. L. D. (1999). A solution-adaptive upwind scheme for ideal magnetohydrodynamics. *Journal of Computational Physics*, 154(2), 284–309. <https://doi.org/10.1006/jcph.1999.6299>

Ridley, A.J., Gombosi, T., & DeZeeuw, D.L. (2004). Ionospheric control of the magnetosphere: Conductance. *Annales Geophysicae*, 22(2), 567–584. <https://hal.archives-ouvertes.fr/hal-00317238/>

Ridley, A.J., D.L. De Zeeuw, & L. Rastätter, (2016). Rating global magnetosphere model simulations through statistical data-model comparisons. *Space Weather*, 14 (10), 819–843. <https://doi.org/10.1002/2016SW001465>

Singer, B. S., B. R. Jicha, N. Mochizuki, R. S. Coe. (2019). Synchronizing volcanic, sedimentary, and ice core records of Earth's last magnetic polarity reversal, *Science Advances*, 5, eaaw4621. <https://www.science.org/doi/10.1126/sciadv.aaw4621>

Siscoe, G. L. & Chen, C.-K. (1975). The paleomagnetosphere. *Journal of Geophysical Research*, 80, 4675–4680. <https://doi.org/10.1029/JA080i034p04675>

Stadelmann, A., Vogt, J., Glassmeier, K.-H., Kallenrode, M.-B., & Voigt, G.-H. (2010). Cosmic ray and solar energetic particle flux in paleomagnetospheres. *Earth Planets Space*, 62(5), 333–345. <https://doi.org/10.5047/eps.2009.10.002>

Tarduno, J. A., Blackman, E. G., Mamajek E. E. (2014). Detecting the oldest geodynamo and attendant shielding from the solar wind: Implications for habitability. *Physics of the Earth and Planetary Interiors*, 233, 68-87. <https://doi.org/10.1016/j.pepi.2014.05.007>

Tarduno, J. A., Cottrell, R. D., Watkeys, M. K., Hofmann, A., Doubrovine, P. V., Mamajek, E. E., et al. (2010). Geodynamo, solar wind, and magnetopause 3.4 to 3.45 billion years ago. *Science*, 327, 1238–1240. <https://doi.org/10.1126/science.1183445>

Tsareva, O. O. (2019). Generalization of Störmer theory for an axisymmetric superposition of dipole and quadrupole fields. *Journal of Geophysical Research: Space Physics*, 124, 2844–2853. <https://doi.org/10.1029/2018JA026164>

Tóth, G., Sokolov, I. V., Gombosi, T. I., Chesney, D. R., Clauer, C. R., De Zeeuw, D. L., et al. (2005). Space weather modeling framework: A new tool for the space science community. *Journal of Geophysical Research*, 110, A12226. <https://doi.org/10.1029/2005JA011126>

Tóth, G., van der Holst, B., Sokolov, I. V., de Zeeuw, D. L., Gombosi, T. I., Fang, F., et al. (2012). Adaptive numerical algorithms in space weather modeling. *Journal of Computational Physics*, 231, 870–903. <https://doi.org/10.1016/j.jcp.2011.02.006>

Valet, J. P., & Fournier, A. (2016). Deciphering records of geomagnetic reversals. *Reviews of Geophysics*, 54, 410–446. <https://doi.org/10.1002/2015RG000506>

Valet, J. P., Fournier, A., Courtillot, V., & Herrero-Bervera, E. (2012). Dynamical similarity of geomagnetic field reversals. *Nature*, 490(7418), 89–93. <https://doi.org/10.1038/nature11491>

Author Manuscript

Vanhamäki, H., Yoshikawa, A., Amm, O., & Fujii, R. (2012). Ionospheric Joule heating and Poynting flux in quasi-static approximation. *Journal of Geophysical Research*, 117, A08327. <https://doi.org/10.1029/2012JA017841>

Vogt, J., & Glassmeier, K.-H. (2000). On the location of trapped particle populations in quadrupole magnetospheres. *Journal of Geophysical Research*, 105(A6), 13063–13071. <https://doi.org/10.1029/2000JA900006>

Vogt, J., & Glassmeier, K.-H. (2001). Modelling the paleomagnetosphere: Strategy and first results. *Advances in Space Research*, 28, 863–868. [https://doi.org/10.1016/S0273-1177\(01\)00504-X](https://doi.org/10.1016/S0273-1177(01)00504-X)

Vogt, J., Zieger, B., Stadelmann, A., Glassmeier, K.-H., Gombosi, T. I., K. Hansen, C., & Ridley, A. J. (2004). MHD simulations of quadrupolar paleomagnetospheres. *Journal of Geophysical Research: Space Physics*, 109, A12221. <https://doi.org/10.1029/2003JA010273>

Vogt, J., Zieger, B., Glassmeier, K.-H., Stadelmann, A., Kallenrode, M.-B., Sinnhuber, M., & Winkler, H. (2007). Energetic particles in the paleomagnetosphere: Reduced dipole configurations and quadrupolar contributions. *Journal of Geophysical Research*, 112, A06216. <https://doi.org/10.1029/2006JA012224>

Wang, C., Han, J. P., Li, H., Peng, Z., & Richardson, J. D. (2014). Solar wind-magnetosphere energy coupling function fitting: Results from global MHD simulation. *Journal of Geophysical Research: Space Physics*, 119, 6199–6212. <https://doi.org/10.1002/2014JA019834>

Wang, H., Lühr, H., Ridley, A., Ritter, P., & Yu, Y. (2008). Storm time dynamics of auroral electrojets: CHAMP observation and the Space Weather Modeling Framework comparison. *Annales Geophysicae*, 26, 555-570. <https://doi.org/10.5194/angeo-26-555-2008>

Wang, H., Zhang, J., Lühr, H., & Wei, Y. (2017). Longitudinal modulation of electron and mass densities at middle and auroral latitudes: Effect of geomagnetic field strength. *Journal of Geophysical Research: Space Physics*, 122, 6595–6610. <https://doi.org/10.1002/2016JA023829>

Wei Y., Pu, Z., Zong, Q., Wan, W., Ren, Z., Fraenz, M., et al. (2014). Oxygen escape from the Earth during geomagnetic reversals: Implications to mass extinction. *Earth and Planetary Science Letters*, 394, 94-98. <https://doi.org/10.1016/j.epsl.2014.03.018>

Winch, D. E., Ivers, D. J., Turner, J. P. R., Stening, R. J. (2005). Geomagnetism and Schmidt quasi-normalization. *Geophysical Journal International*, 293, 160(2): 487–504. <https://doi.org/10.1111/j.1365-246X.2004.02472.x>

Yu, Y., & Ridley, A. J. (2008). Validation of the space weather modeling framework using ground-based magnetometers. *Space Weather*, 6, 05002. <https://doi.org/10.1029/2007SW000345>

Yu, Y., Ridley, A. J., Welling, D. T., & Tóth, G. (2010). Including gap region field-aligned currents and magnetospheric currents in the MHD calculation of ground-based magnetic field perturbations. *Journal of Geophysical Research*, 115, A08207. <https://doi.org/10.1029/2009JA014869>

Yu, Y., Jordanova, V., Zou, S., Heelis, R., Ruohoniemi, M., & Wygant, J. (2015). Modeling subauroral polarization streams during the 17 March 2013 storm. *Journal of Geophysical Research*, 120, 1738-1750. <https://doi.org/10.1002/2014JA020371>

Yu, Y., J. Cao., H. Fu., H. Lu., and Z. Yao. (2017). The effects of bursty bulkflows on global-scale current systems. *Journal of Geophysical Research: Space Physics*, 122, <https://doi.org/10.1002/2017JA024168>

Zieger, B., Vogt, J., Glassmeier, K.-H., & Gombosi, T. I. (2004). Magnetohydrodynamic simulation of an equatorial dipolar paleomagnetosphere.

Journal of Geophysical Research: Space Physics, 109, A07205.  
<https://doi.org/10.1029/2004JA010434>

Zieger, B., Vogt, J., Ridley, A. J., & Glassmeier, K.-H. (2006a). A parametric study of magnetosphere–ionosphere coupling in the paleomagnetosphere. *Advances in Space Research*, 38, 1707–1712. <https://doi.org/10.1016/j.asr.2005.04.077>

Zieger, B., Vogt, J., & Glassmeier, K.-H. (2006b). Scaling relations in the paleomagnetosphere derived from MHD simulations. *Journal of Geophysical Research: Space Physics*, 111, A06203. <https://doi.org/10.1029/2005JA011531>

## Figure caption

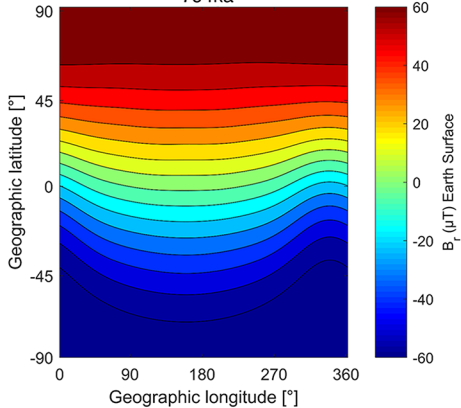
**Figure 1.** The global geomagnetic field distribution during the M-B reversal period using the data-reconstructed model “IMMAB4” (Leonhardt & Fabian, 2007). The X-axis and Y-axis represent geographic longitude and latitude, respectively.

**Figure 2.** The left column displays the 3D view of the magnetopause surface at different phases during the M-B reversal; the right column shows the magnetic field lines in the magnetosphere. The red lines represent magnetic field lines being reconnected, projected into the  $Y=0$  plane. Color in the magnetosphere represents plasma density in  $\text{amu}/\text{cm}^3$ . Color on the Earth surface is the magnitude of the geomagnetic field.

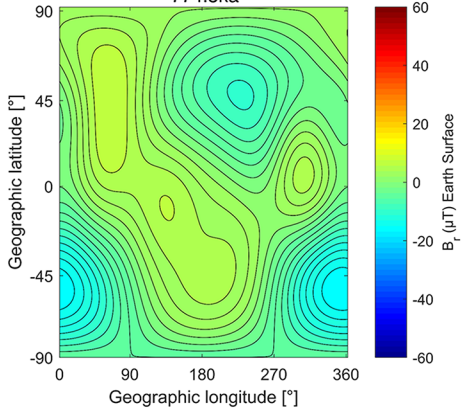
**Figure 3.** The temporal evolution of (a) the stand-off distance of subsolar point (in unit of  $R_e$ ), (b) total solar wind power gain through the magnetopause surface ( $\text{SWP}_{\text{m.p.}}$ , in unit of Watt), (c) the effective solar wind power ( $\text{SWP}_e$ ) (blue line, in unit of Watt), the geomagnetic dipole moment (red line, in unit of  $\text{A m}^2$ ), and the present value of the geomagnetic dipole moment in 2020 (black line, in unit of  $\text{A m}^2$ ), and (d) the ratio between  $\text{SWP}_{\text{m.p.}}$  and  $\text{SWP}_e$ , which represents the solar wind energy input efficiency. We divide the entire M-B reversal process into three phases with the vertical red lines: pre-reversal phase before 779 ka, reversal phase (779ka - 769ka), and post-reversal phase after 769 ka. The small figure in (b) is the geomagnetic power spectrum of different components. The black and red lines represent the dipole component and the quadrupole component, respectively. The light red and green regions represent before and after the polarity reversal of the dipole component.

**Figure 4.** In the northern hemisphere, both projected field-aligned currents (FACs)  $J_{\parallel}$  (left) and Poynting flux (right) are from 776 ka to 768 ka in chronological order. The Red represents downward Poynting flux, the blue represents upward Poynting flux. The black circles are latitudes mapped to the altitude of the  $2.5 R_e$ .

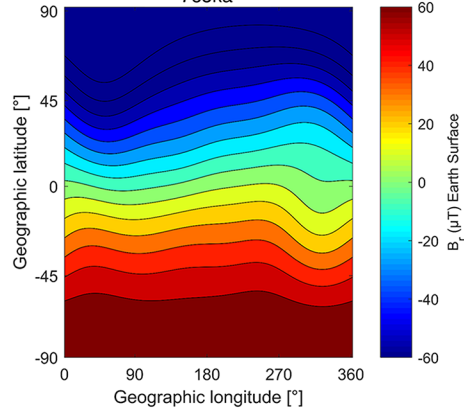
Magnetic field  
794ka



Magnetic field  
774.5ka

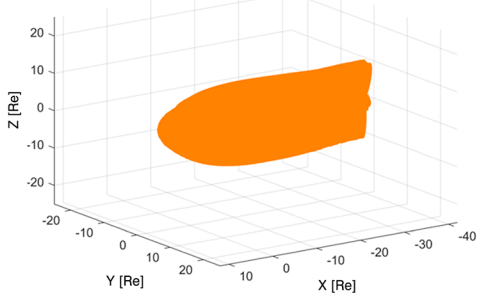


Magnetic field  
765ka

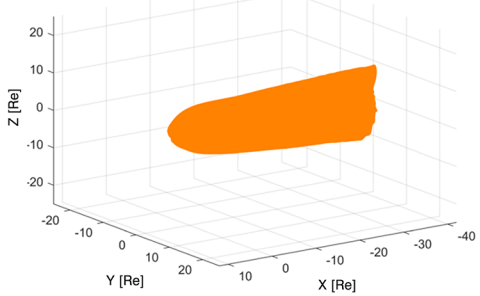




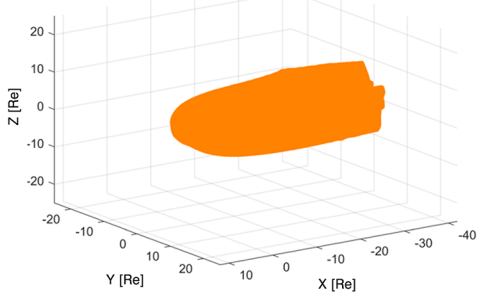
776.0ka



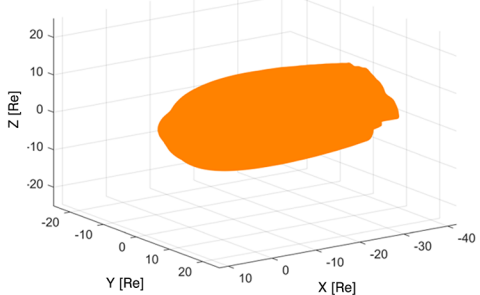
774.5ka



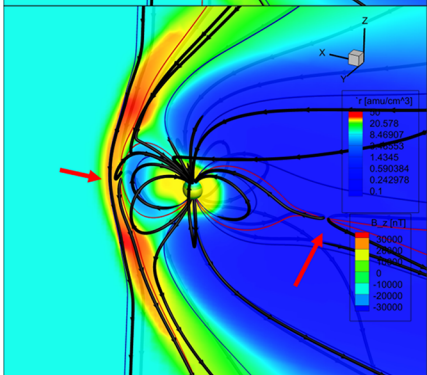
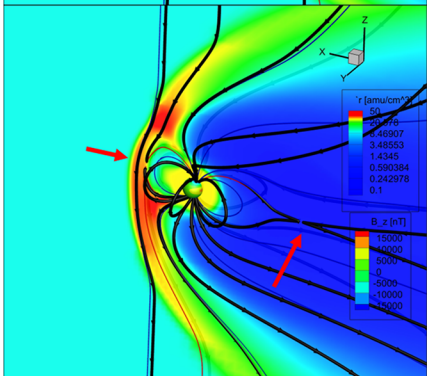
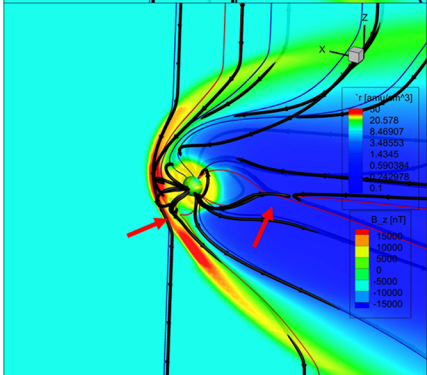
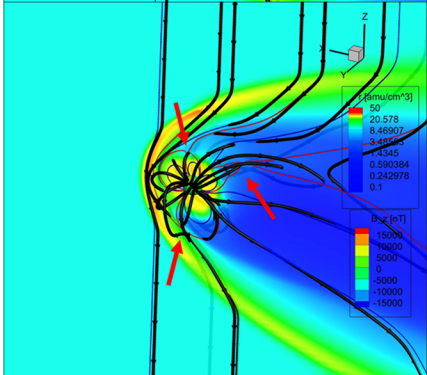
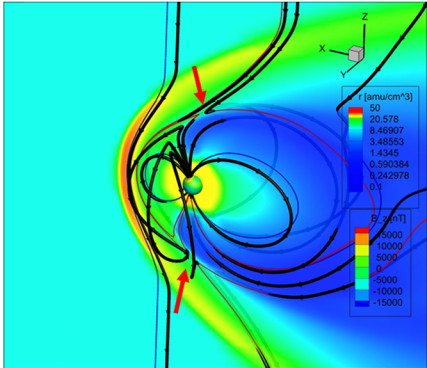
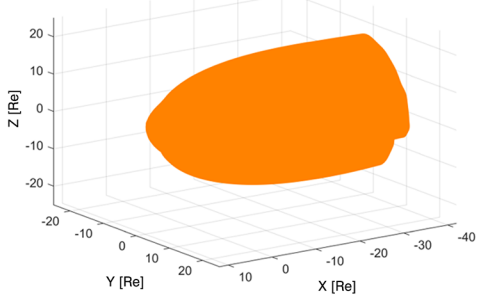
774.2ka

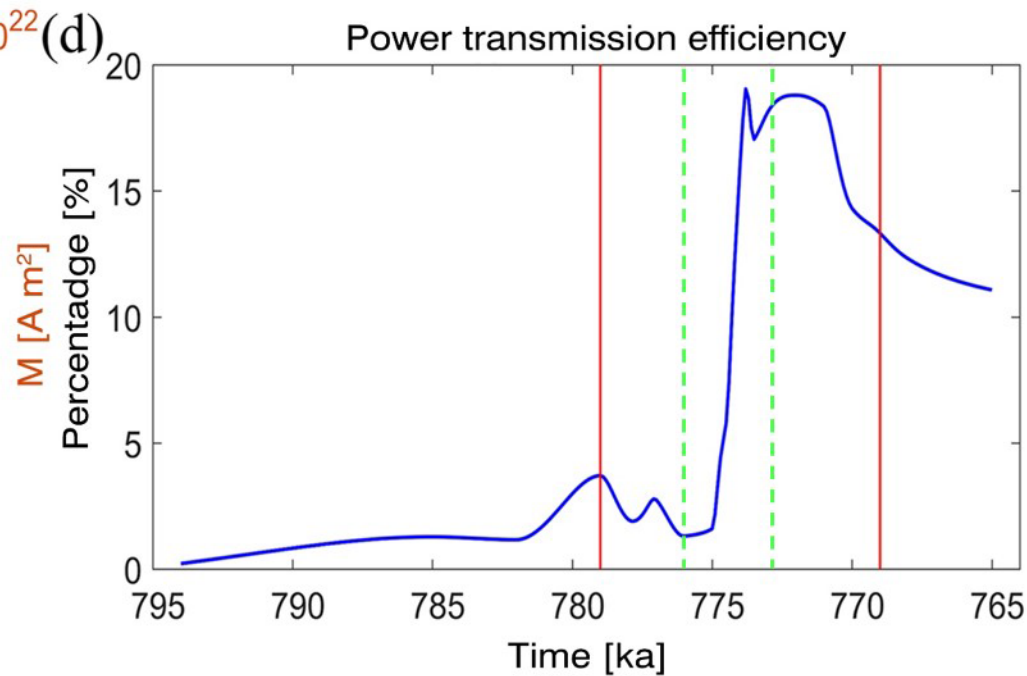
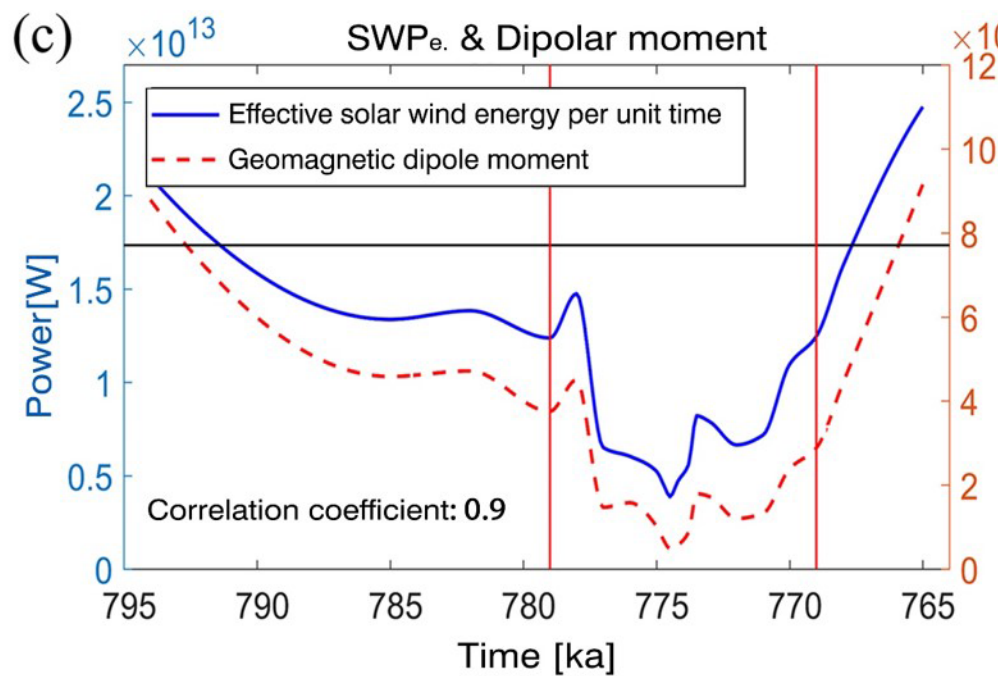
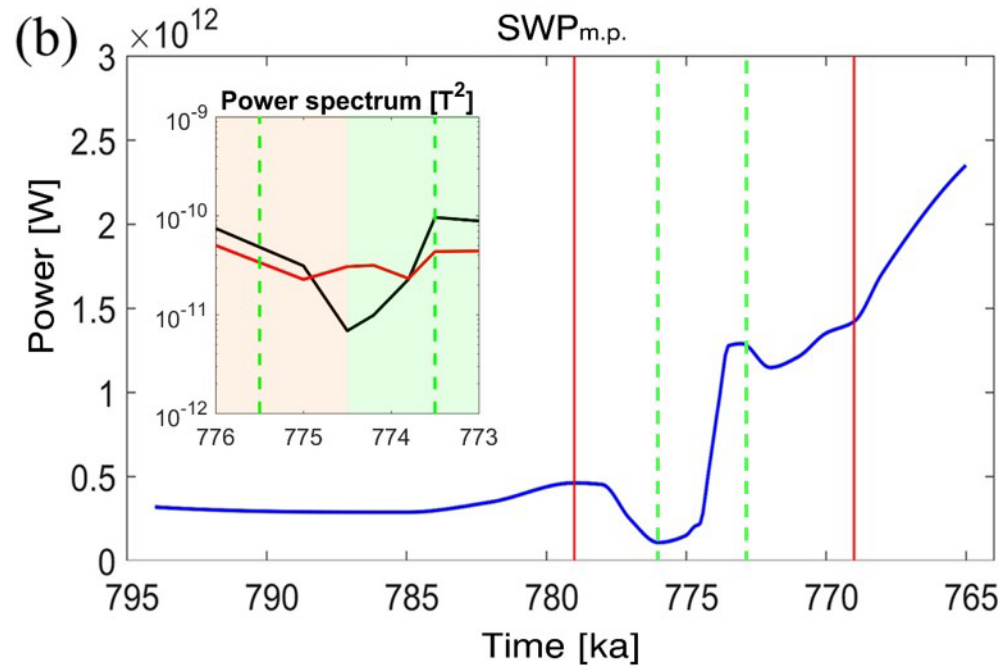
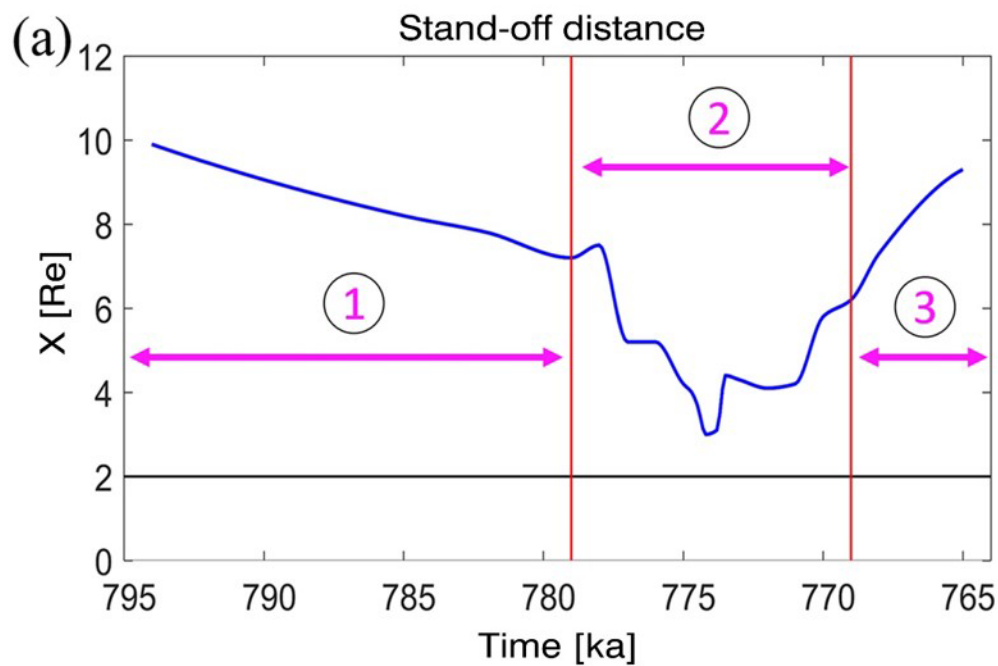


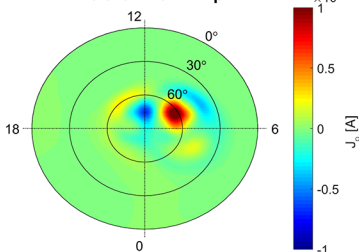
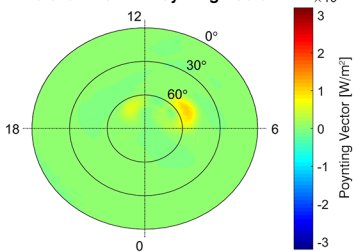
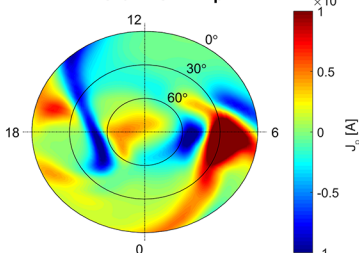
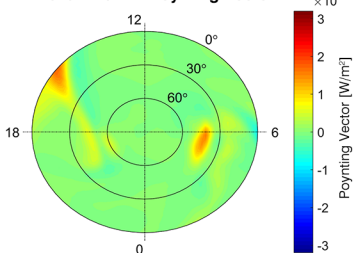
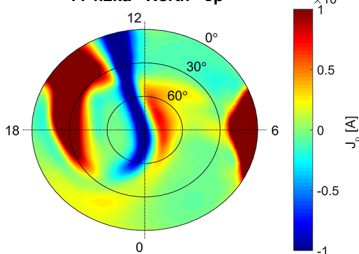
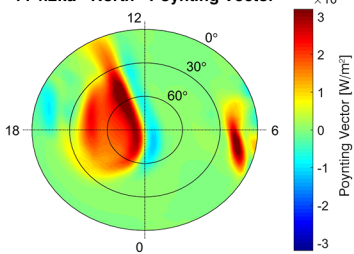
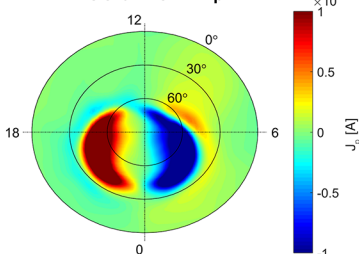
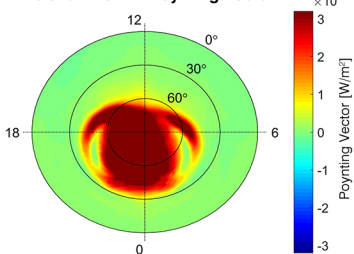
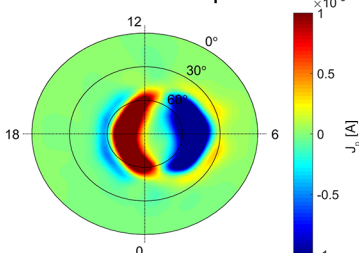
773.5ka



768.0ka





**776.0ka North Jp****776.0ka North Poynting Vector****774.5ka North Jp****774.5ka North Poynting Vector****774.2ka North Jp****774.2ka North Poynting Vector****773.5ka North Jp****773.5ka North Poynting Vector****768.0ka North Jp****768.0ka North Poynting Vector**